Distributed Fibre Optic Sensing of Axially Loaded Bored Piles

Loizos Pelecanos[1], Kenichi Soga[2], Mohammed Z. E. B. Elshafie[3], Nicholas de Battista[4],

Cedric Kechavarzi[5], Chang Ye Gue[6], Yue Ouyang[7], Hyung-Joon Seo[8]

[1] Lecturer in Geotechnical Engineering, Department of Architecture & Civil Engineering, University of Bath. Claverton Down, Bath, BA2 7AY, United Kingdom. Formerly: Research Associate, University of Cambridge, United Kingdom. Email: L.Pelecanos@bath.ac.uk. (Corresponding Author).

[2] Chancellor's Professor of Civil Engineering, Department of Civil & Environmental Engineering, University of California, Berkeley. 760 Davis Hall, 94720-1710, United States of America. Formerly: Professor, University of Cambridge, United Kingdom. Email: Soga@berkeley.edu

[3] Lecturer in Construction Engineering, Centre for Smart Infrastructure & Construction, Department of Engineering, University of Cambridge. Trumpington Street, Cambridge, CB2 1PZ, United Kingdom. Email: ME254@cam.ac.uk

[4] Research Associate, Centre for Smart Infrastructure & Construction, Department of Engineering, University of Cambridge. Trumpington Street, Cambridge, CB2 1PZ, United Kingdom. Email: N.Debattista@eng.cam.ac.uk

[5] Training & Knowledge Transfer Manager, Centre for Smart Infrastructure & Construction, Department of Engineering, University of Cambridge. Trumpington Street, Cambridge, CB2 1PZ, United Kingdom. Email: CK209@cam.ac.uk

[6] PhD Research Student, Centre for Smart Infrastructure & Construction, Department of Engineering, University of Cambridge. Trumpington Street, Cambridge, CB2 1PZ, United Kingdom. Email: CYG20@cam.ac.uk

[7] Project Manager, Cementation Skanska. Formerly: University of Cambridge, United Kingdom. Neelands House, Pipering Lane, Doncaster, DN5 9NB, United Kingdom. Email: Echo.Ouyang@skanska.co.uk

[8] Lecturer, Department of Civil Engineering, Xi'an Jiaotong – Liverpool University, Shaanxi Sheng, China, 710048, China. Formerly: Research Associate, University of Cambridge, United Kingdom. Email: Hyungjoon.Seo@xjtlu.edu.cn

Abstract

Instrumented pile tests are vital to establish the performance of a pile and validate the assumptions made during initial design. Conventional instrumentation includes vibrating wire strain gauges and extensometers to measure the change in strain or displacements within a pile. While these strain and displacement gauges are very accurate, they only provide strain/displacement readings at discrete locations at which they are installed. It is therefore common to interpolate between two consecutive points to obtain the values corresponding to the data gaps in between; in practice, these discrete instrumented points could be tens of

30   meters apart, at depths corresponding to different soil layers, and hence simple interpolation

31   between the measurement points remains questionable. The Brillouin Optical Time Domain

32   Reflectometry fibre optic strain sensing system however is able to provide distributed strain

33   sensing along the entire length of the cable, enabling the full strain profile to be measured

34   during a maintained pile load test. The strain data can also be integrated to obtain the

35   displacement profile. In this paper, three case studies are presented where the performance

36   of three concrete bored piles in London is investigated using both conventional vibrating wire

37   strain gauges and distributed fibre optic strain sensing during maintained pile load tests

38   which enabled comparisons to be made between the two instrumentation systems. In

39   addition, finite element analyses were conducted for the three piles and it was found that the

40   ability to measure the full strain profiles for each pile is highly advantageous in

41   understanding the performance of the pile and in detecting any abnormalities in the pile

42   behaviour.

43   **Keywords:** piles, field monitoring, fibre optic sensors, load transfer, pile load test, finite element analysis, pile instrumentation

1. Introduction

45   The overall geotechnical capacity of a pile is derived from the skin friction and the base

46   resistance. The design process begins with evaluating moderately conservative soil

47   parameters based on site investigation test results. Depending on the type of soil, different

48   equations and methods for pile capacity can be used. For example, for piles in clay the α-

49   method and the method proposed by Meyerhof (1965) are commonly used (e.g. in the UK)

50   to predict the ultimate skin friction and end bearing resistance respectively. Other methods

51   adopt direct correlations based on in situ soil investigation (e.g. CPT, SPT) (Eslami &

52   Fellenius 1997), LCPC (Bustamante & Gianeselli 1982), IC method (Jardine & Chow 1996).

53   More complex and rigorous numerical methods can also be employed for complicated pile

54   problems such as piled groups (Kraft, Ray & Kakaaki 1981; Poulos 1989; Randolph 2003)

55   and piled raft (Poulos & Davis 1974; Kitiyodom & Matsumoto 2003) foundations.

56   Nevertheless, all of these methods are used in the design stage and therefore they only

57 provide an estimate of a pile's behaviour. As such, instrumented pile tests are recommended

58 by standard codes of practice (e.g. clause 7.5 of Eurocode 7) to quantify the performance of

59 a pile in order to validate the initial design assumptions.

60 General preliminary pile tests (McCabe & Lehane 2006) include a number of vibrating wire

61 strain gauges (VWSG), either in pairs or threes at several levels within the pile, along with a

62 measurement of pile head settlement measured from an independent reference beam by

63 linear voltage distance transducers (LVDT). This instrumentation scheme offers very useful

64 but discrete data points (Lehane et al. 1993). Data from appropriately monitored pile load

65 tests can provide a means to assess the behaviour of the pile and develop pile behaviour

66 models (Comodromos & Bareka 2009) such as load transfer curves (Ménard 1963;

67 Butterfield & Banergee 1971; Kraft, Ray & Kakaaki 1981; Frank & Zhao 1982; Poulos 1989;

68 Lee 1993; Klar et al. 2006; Abchir et al. 2015; Seo et al. 2017).

69 Recent advances in geotechnical instrumentation include fibre optic (FO) technology such as

70 Fibre Bragg Gratings (FBG) (Kersey & Morey 1993; Lee et al. 2004; Liu & Zhang 2012;

71 Doherty et al. 2015) and distributed Brillouin Optical Time-Domain Reflectometry (BOTDR)

72 (Kurashima et al. 1993; Soga 2014; Pelecanos et al. 2017). The latter technology offers near

73 spatially-continuous strain data along the entire length of the pile, which can be further

74 processed to provide detailed information regarding the pile behaviour and integrity and

75 load-transfer properties (Pelecanos & Soga 2017; de Battista et al. 2016). The BOTDR

76 technique has been successfully used to monitor various soil-structure interaction problems

77 (Acikgoz et al. 2016; Acikgoz et al. 2017), including piles (Klar et al. 2006; Ouyang et al.

78 2015; Pelecanos et al. 2016), shafts/retaining walls (Mohamad et al. 2011; Schwamb et al.

79 2014; Schwamb & Soga 2015), tunnel linings (Mohamad et al. 2010; Mohamad et al. 2012;

80 Cheung et al. 2010; de Battista et al. 2015; Di Murro et al. 2016; Soga et al. 2017), tunnelling

81 and other geotechnical process-induced surface settlements (Hauswirth et al. 2014; Klar,

82 Dromy & Linker 2014; Linker & Klar 2015), concrete cracking (Goldfeld & Klar 2013), soil

83 slopes etc.

84 In this paper the BOTDR distributed monitoring technology is briefly discussed and its

85 application in a number of pile load test cases (both top-loaded using an external reference

86 frame and bi-directionally loaded using an Osterberg-cell) in London is explored. The

87 monitoring data from the distributed BOTDR and discrete VWSG technologies in the three

88 case studies is analysed and compared to shed light on the relative merits of each approach

89 (continuous and discrete) and highlight their necessity in future reliable pile load testing.

90 Finally, numerical analyses were conducted for each of the three piles and the results are

91 presented in this paper to enable a better understanding of pile behaviour under loading.

92 **2. Distributed fibre optic monitoring**

93 This section provides a brief description of the principles of BOTDR. However, the complete

94 description of the method and the associated experimental approaches required for

95 calibration are well beyond the scope of this paper and they are therefore not included, as

96 they can be found elsewhere in great detail (Mohamad 2007; Iten 2011; Soga 2014; Soga et

97 al. 2015). More information about the fundamentals of light propagation can be obtained

98 from relevant literature in the area of photonics (Horiguchi et al. 1995) as this is out of scope

99 of this paper. A detailed description of the theory of distributed FO strain sensing and its

100 applications in civil and geotechnical infrastructure is given by Kechavarzi et al. (2016)

101 **2.1. Principle of Brillouin Optical Time Domain Reflectometry**

102 A fibre optic (FO) cable allows light waves from a FO analyser to travel along its entire length

103 through total internal reflection, irrespective of the orientation of the cable itself. This allows a

104 signal to be carried over very long distances, such as for broadband Internet. Backscattered

105 signals are generated as the light wave passes through the optical fibre and presents itself

106 as Rayleigh, Raman and Brillouin spectrum. Within the Brillouin backscatter, it is found that

107 the peak frequency experiences a shift that is generally considered to be linearly

108 proportional to applied strain. Using the measured time required for the backscattered signal

109 to return to the analyser, the specific location at which this frequency shift is observed can

110   be estimated accurately. Therefore, the entire fibre optic cable is essentially serving as a

111   distributed strain sensor.

112   The FO analyser sends a light with of 1550 nm wavelength into an optical fibre and the

113   generated Brillouin spectrum of the back-scattered light has 25-27 MHz bandwidth and

114   around 11 GHz central peak frequency when no strain is applied on the fibre. The back-

115   scattered Brillouin central frequency, v_b, is related to the input light according to Eq. 1 and

116   this is provided directly from the FO analyser.

117

$$v_b = \frac{2 \cdot n_f \cdot v_a}{\lambda_l}$$

118   **Eq. 1**

119   where n_f is the fibre core refractive index, v_a is the acoustic velocity in the fibre and λ_l is the

120   wave length of the input light.

121   Changes in temperature and/or strain induce a density change in the cable and therefore

122   change in the acoustic velocity, v_a, of the light too. As the strain or temperature at a given

123   location change, the frequency of the backscattered light is shifted by an amount which is

124   approximately linearly proportional to the applied strain, $\Delta\varepsilon$, or temperature, ΔT, according to

125   Eq. 2.

126

$$\Delta v_b = \Delta v_{b0} + M \cdot \Delta\varepsilon + N \cdot \Delta T$$

127   **Eq. 2**

128   Where, v_{b0} is the central Brillouin peak frequency at zero strain and at a given temperature,

129    $\Delta\varepsilon$ is the applied strain, ΔT is the temperature change, and M, N are the coefficients for

130   strain and temperature change respectively. For an incident wavelength of 1550nm, the

131   Brillouin frequency shift can vary from 9GHz to 13GHz depending on the different fibre

132   properties. Therefore knowledge about of this frequency difference can provide information

133   about the applied strain and temperature changes at the location where the back-scattered

134   light was generated. As the speed of light is constant, the location can be evaluated by

135 measuring the time since the light was initially sent into the fibre. Back-scattered light is

136 generated at every point along the entire length of the fibre and therefore by resolving both

137 time and frequency a continuous strain profile along the fibre can be determined.

138 For the case studies presented in this paper, either the AQ8603 analyser manufactured by

139 Yokogawa Electric Corporation, Japan, or the NeubreScope NBX-5000 analyser

140 manufactured by Neubrex, Japan, are employed. These are able to provide a minimum

141 readout resolution between 0.05m and 0.1m with a spatial resolution of 0.5 to 1.0m. Spatial

142 resolution implies that it produces a weighted average strain reading over 0.5 or 1m at every

143 0.05m length of the cable (this is considered as "spatially-continuous" or "distributed" data).

144 These settings can be changed depending on the time allocated for the specific test.

145 Essentially the technology offers a large number of strain data (every 0.05m to 0.1m in this

146 case) along a structure embedded with fibre optic cables.

147 In addition to the clear advantage of measuring a full strain profile, its simplicity lies in the

148 fact that only a single cable is required for the entire system, enabling its use in small

149 diameter piles and eliminating the time and effort for cable management, that would be

150 required for conventional strain gauges. No electricity is required other than to power the

151 analyser itself, which could be located much further away in a safe, and convenient location

152 on the construction site, as light waves travel efficiently through the fibre optic cables. The

153 result is an instrumentation system which can provide a full strain profile of the pile.

154   **2.2. Fibre Optic Cables**

155 Strain on an optical fibre can be generated from two sources, mechanical or thermal.

156 Therefore, two types of optical fibre cables are installed and are shown in Figure 2: Fujikura

157 4-core single mode fibres reinforced ribbon cable for strain sensing (strain sensing cable)

158 and Excel 4-core single mode fibres loose tube for temperature compensation (temperature

159 cable). While they are both attached to the reinforcement cage, the fibre optic cores of the

160 temperature cable sit in a gel which isolates any transfer of mechanical strains from the

161 outer coating. Thus it is only subjected to thermal changes. These measurements are used

162 to compensate the readings measured from the strain cables to provide an accurate reading

163 of interest, the actual mechanical strain.

164   **2.3. Installation of FO Instrumentation**

165 Installation of FO cables is usually done on site, as described in Figure 3. Long pile

166 foundations typically consist of a number of steel reinforcement cage segments and

167 therefore the bottom steel cage is instrumented on the ground. The FO cables (shown in

168 blue colour in Figure 3) are running along the entire length of the bottom segment on two

169 opposite sides of the pile and a loop of some FO cable is made close to the bottom of the

170 segment. The longitudinal cables are pre-strained (i.e. a tensile strain is applied) using cable

171 clamps at the two ends of the steel cage. Once the borehole is dug, the bottom cage is

172 inserted and while the other cages are spliced onto the bottom cage and the whole pile

173 lowered down in the borehole, the remaining FO cable is attached to them. Finally, the two

174 ends of the FO cable run from the top of the pile to the FO analyser.

175 With the pile loaded axially, it is assumed that the concrete pile will have negligible hoop

176 strain across its cross section and therefore a 10m loop cable for both strain and

177 temperature is prepared and secured at the end of the bottom reinforcement cage to serve

178 as a zero-strain loop for referencing and compensation purposes.

179 For the ease of data interpretation, a pre-strain of about 1000-2000$\mu\varepsilon$ is often introduced to

180 the strain cable. Anchorage is provided on the bottom loop end by cable wire clamps before

181 stretching the strain cable to the predetermined pre-strain. Strain cable is then secured with

182 another set of cable wire clamps at the top of the reinforcement cage before supplementing

183 the anchorage by either spot gluing with epoxy glue or using cable ties at approximately

184 every 0.5-1.0m interval. Temperature cables are loosely secured next to the strain cables

185 with cable ties as they are routed to the top of the cage. Figure 4 (a) and (b) show the

186 installed FO cables and sister-bar VWSGs on a foundation pile.

187 Once the bottom cage has been instrumented, it is lowered into the borehole. The fibre optic

188 cables are then unwound from the reels on each side of the borehole as the cage is lowered.

189 Pre-straining is carried out for the strain cables for subsequent reinforcement cages as well

190 without epoxy glue due to time constraints. Concrete is subsequently poured in the borehole

191 and as the concrete cures the FO cables become securely embedded within the pile. Further

192 details of FO cable installation in piles established at University of Cambridge can be found

193 in (Klar et al. 2006; Soga 2014; Soga et al. 2015).

194   **2.4. FO data analysis**

195 As described earlier, applied strain causes a shift in the peak Brillouin frequency in the

196 optical fibre. Therefore, by measuring the frequency difference, one can obtain the applied

197 strain on the cable. Moreover, because FO cables are able to detect strains due to both

198 mechanical and thermal loads, the two components need to be analysed separately. The

199 measured frequency difference from the "temperature cable", Δv_{bT}, is influenced only by

200 changes in temperature, whereas that from the "strain cable", Δv_{bS}, is influenced by changes

201 in both mechanical load and temperature.

202 Therefore, changes in temperature, ΔT, can be obtained from Eq. 3 (where, C_{TT} is a

203 property of the cable, obtained by calibrating the "temperature cable", which determines how

204 temperature affects the Brillouin frequency reading of the cable and it is usually around

205 $1.1 \cdot 10^{-3}$ GHz/°C).

$$\Delta T = \frac{\Delta v_{bT}}{C_{TT}}$$

206

207 **Eq. 3**

208 The thermal strain, ε_{temp}, (the strain that corresponds to free thermal expansion strain due to

209 temperature change) is then given by Eq. 4 (where, α_c is the thermal expansion coefficient

210 of concrete and it is usually around 9.65 µε/°C).

$$\varepsilon_{temp} = a_c \cdot \Delta T$$

211

212 **Eq. 4**

213 The real (observed) strain, ε_{real}, (the actual strain that the pile experiences in the field) is then

214 given by Eq. 5 (where, C_E is a property of the fibre, obtained by calibrating the "strain cable",

215 which determines how strain affects the Brillouin frequency and it is usually around $5 \cdot 10^{-4}$

216 GHz/µε; and C_T is a property of the fibre that determines how the Brillouin frequency is

217 affected by temperature difference, and it is usually around $1.0 \cdot 10^{-3}$ GHz/ºC).

218
$$\varepsilon_{real} = \frac{1}{C_E}(\Delta v_{bS} - C_T \cdot \Delta T)$$

219 **Eq. 5**

220 The mechanical (constrained) strain, ε_{mech}, (the reaction strain that is the result of both the

221 applied mechanical load and temperature) is then given by Eq. 6

222
$$\varepsilon_{mech} = \varepsilon_{real} - \varepsilon_{temp} = \frac{1}{C_E}\left[\Delta v_{bS} - C_T \cdot \left(\frac{\Delta v_{bT}}{C_{TT}}\right)\right] - a_c \cdot \frac{\Delta v_{bT}}{C_{TT}}$$

223 **Eq. 6**

224 Finally, once the strain profiles are obtained, the actual geotechnical response of the pile

225 may be captured using Eq. 7 and Eq. 8 to determine axial force, $F_a(y)$, and vertical

226 displacement, u(y), profiles respectively.

227
$$F_a(y) = EA \cdot \varepsilon_{mech}(y)$$

228 **Eq. 7**

229
$$u(y) = u(y = y_0) + \int_0^y \varepsilon_{real}(y)\,dy$$

230 **Eq. 8**

231 Where, EA is the axial rigidity of the pile (E is Young's modulus and A is cross-sectional

232 area) and y is the depth from the top of the pile. For the vertical displacements, the relative

233 displacements obtained from the integration of axial strains is added to available absolute

234 displacement values from displacement transducers at y_0. The data profiles obtained from

235 BOTDR have usually a wavy nature and therefore they need to be filtered prior to data

236 analysis. The data presented in this study have been filtered using a second order Savitzky-

237 Golay (1964) filter with a 31-point frame.

238 **3. Case study 1: Pile load test at Broadgate Road, London.**

239 **3.1. Description of pile test**

240 The Broadgate Road project in London was designed to house a fourteen-storey office

241 building with two basement levels. Due to tight space restrictions along one side of the

242 project, a number of mini piles of 0.305m diameter were constructed in close proximity to

243 support the superstructure. A high-strength steel reinforcing case was inserted in the ground

244 after the drilling process. The pile tested is 0.305m diameter (0.343m at the top 6m because

245 of a steel casing around the pile) and 25m long, as shown in Figure 5 (a). On the same

246 figure, the soil stratigraphy is also included with some known material properties obtained

247 from relevant triaxial and simple shear laboratory tests. The pile test was carried out once

248 the concrete material achieved a specified value of minimum strength. The pile test consists

249 of three consecutive cycles of applied load (at the top of the pile) of up to 720kN, 1080kN

250 and 1985kN for each of the three cycles, achieved after several loading and unloading steps

251 (Figure 5 (b)). The pile was instrumented with distributed FO cables on two opposite sides of

252 the pile and a number of discrete VWSGs along the pile depth.

253 **3.2. Data Interpretation**

254 Figure 6(a) shows the axial strain in the pile for the three peak values of the three cycles as

255 it was captured by the FO cables and the VWSGs, whereas Figure 6(b) shows the

256 corresponding axial force profiles (calculated from strains multiplied by the pile axial rigidity,

257 EA, as described by Eq. 7 and using E=30000MPa. This value adopted for E was obtained

258 following the Fellenius (1989) approach and by using the FO strain values, ε, at the top

259 30cm of the pile (surrounded by soil but with insignificant influence, see Figure 6a, Figure

260 9a, Figure 12a) and the applied loads, P, ($E=\Delta P/\Delta\varepsilon/A$). The Fellenius method proposes a

261 smooth linear (best-fit) reduction of secant modulus with axial strains. Therefore, a

262 representative average value of E over the dominant experienced strains (~300-700$\mu\varepsilon$) was

263 adopted based on that best-fit line. It is shown that there is a generally good agreement

264 between the two monitoring technologies. No VWSG data were obtained for the largest cycle

265 (i.e. for loading of 1985kN), as there was a malfunction of the VWSG instruments, and

266 therefore only FO data is available for this load case. It is also shown that there is some

267 scatter in the FO data values which is currently a known issue with distributed FO strain

268 sensing systems. This is because the standard resolution of FO is constant and about 30-

269 50$\mu\varepsilon$ and therefore this becomes relatively less significant for larger applied loads (which

270 imply larger induced strains). The waviness of FO strains may offer a challenge when

271 differentiating strain data profiles to obtain shaft friction values, but their spatial continuity

272 allows for a distributed sensing of localised strains, e.g. necking, fracture etc., whereas, such

273 localised features would not be identified by discrete monitoring systems (such as VWSGs).

274 Figure 6(c) shows the vertical displacements, u, of the pile from the FO cables. The values

275 from the FOs were obtained by integrating the strain profiles and adding those to absolute

276 displacement measurements from displacement transducers at the top of the pile, as

277 described by Eq. 8.

278 The results of a simplified numerical finite element (FE) beam-spring model are included for

279 comparison in Figure 6. The simplified FE analysis considered a single vertical pile loaded

280 axially from the top modelled with linear beam elements and represented the surrounding

281 soil with non-linear springs which is a practical approach as opposed to the more common

282 way of modelling the soil with solid elements. All the beam elements and non-linear springs

283 contribute to the global stiffness matrix and therefore the global FE equilibrium equations.

284 Due to the nonlinear nature of the soil-spring the external load is applied incrementally and

285 the equations are solved using an iterative Modified Newton-Raphson technique. A number

286 of different soil layers, associated with constant soil spring properties along the depth of

287 each layer, were considered based on the ground conditions, although they did not follow

288 exactly the soil stratigraphy. This simplified FE analysis approach is explained in the

11

289   Appendix in more detail. The behaviour of the pile was back-analysed to derive the

290   properties of the soil springs which are subsequently used in the FE analysis to calculate the

291   axial strain and vertical displacement profiles. Namely, the optimum set of properties of the

292   soil springs was obtained that was able to reproduce well the observed axial strain and

293   vertical displacement profiles from the FO readings. The values of the model parameters

294   was obtained through a simple optimisation algorithm (here the Levenberg-Marquardt

295   scheme was used (Levenberg 1944; Marduardt 1963)), in which the changing variables were

296   the set of the model parameters (i.e. in this case 20 parameters, 4 for each of the 4 layers

297   and 1 for the pile base) and the objective function was the difference of the axial strains

298   obtained from the numerical model and those observed from the FOs. It is shown here that a

299   good match is obtained between the field data (from FO & VWSGs) and the FE back-

300   calculations.

301   Figure 7 (a) shows the calculated shaft friction (SF) profiles for the three peak values of the

302   three cycles, from the FE analysis. Since the FO data exhibit some (inherent) undulations,

303   deriving SF values from the slope of the axial force might be cumbersome. Therefore, here a

304   "synthetic" approach is followed, where a numerical model is established that reproduces

305   accurately the monitored axial strain and vertical displacements from FOs (see Figure 6) and

306   then SF profiles are obtained from the FE analysis of the model. This numerical analysis

307   approach was followed here due to the inability to obtain SF values directly from the wavy

308   FO strains. In fact, direct estimation of SF requires differentiation of axial strains which in the

309   case of wavy strain profiles leads to unrealistically large fluctuations of SF values with the

310   depth of the pile. It is shown here that generally larger SF values are obtained within the

311   London Clay stratum (i.e. at z<-4m) as compared to the SF observed at the top soil layers

312   (i.e. at z>-4m). However, it is shown that at the bottom of the pile, very small SF values are

313   mobilised, perhaps due to the small strains experienced by the pile. Since a numerical

314   optimisation procedure was followed to obtain the SF, the small values of strains

315   experienced at the bottom of the pile compared to the usual variation of FO strain data leads

316 to a large noise-to-signal-ratio and therefore the evaluation of SF (i.e. determination of the

317 actual slope of the strain profiles) values may become cumbersome.

318 Furthermore, Figure 7 (b)(c) show the evolution of SF with the applied load, P, and the 'local'

319 vertical displacement, u, at various depths (according to the local soil stratigraphy) along the

320 pile and the pile base pressure, q_b. Figure 7 shows that SF is mobilised early in the test,

321 whereas the pile base pressure is mobilised at later stages for higher loads. As expected the

322 SF development curves show an initial stiffness that drops with the displacement, due to the

323 plasticity of the soil close to the pile shaft. It is clearly observed that the first layer (0-6m),

324 which is covered by the pile casing does not show significant development of strains and

325 approximately reaches an ultimate value of SF of about 20kPa. Besides, although the three

326 layers considered within the London Clay show variable SF development, it is accepted that

327 the majority of the London Clay reaches SF of about 70-100kPa, whereas the bottom of the

328 London Clay shows minimal development of SF. However, this could probably be due to the

329 small layer thickness considered in the data analysis (FO data exist in layer 4 between y=19-

330 22.5m). Nevertheless, in general, the evolution of shaft friction with the vertical

331 displacements seems to reach (roughly) a plateau for displacements of about 0.01-0.03m

332 which is slightly less than 10% of the pile diameter.

333 Finally, Figure 7 (d) shows the relevant design t-z and q-z curves following the API (2002)

334 methodology (see Appendix B). Although there are some differences between the observed

335 (Figure 7 (c)) and design (Figure 7 (d)) curves, in general they seem to agree quite well

336 yielding comparable values of ultimate pile shaft and base resistance.

337 ### 3.3. Remarks

338 A typical interpretation of the geotechnical data would consider Eq. 9 and Eq. 10 to

339 calculate the ultimate shaft capacity, q_s, and Eq. 11 and Eq. 12 for the base capacity, q_b of

340 the pile (Salgado 2008; Knappett & Craig 2012; Tomlinson & Woodward 2014).

341
$$q_{s(cohesive)} = \alpha \cdot S_u$$

342 **Eq. 9**

343 $$q_{s(non-cohesive)} = \beta \cdot \sigma'_{vo} = K_o \cdot \tan \delta \cdot \sigma'_{vo}$$

344 **Eq. 10**

345 $$q_{b(cohesive)} = N_c \cdot S_u$$

346 **Eq. 11**

347 $$q_{b(non-cohesive)} = N_q \cdot \sigma'_{vo}$$

348 **Eq. 12**

349 where, α (usually around 0.5 for London Clay (Tomlinson 1997)) is the empirical shaft

350 coefficient, K_o is the earth pressure at rest, δ (usually around 0.75φ) (Stas & Kulhawy 1984)

351 is the pile-soil interface friction angle and N_q (usually around 50 (Berezantzev, Khristoforov &

352 Golubkov 1961; Knappett & Craig 2012)) and N_c (usually its value is taken as 9 (Kulhawy &

353 Prakoso 1999)) are the base bearing capacity coefficients.

354 Using the above equations and the geotechnical data in Figure 5 one would obtain an

355 ultimate value of shaft capacity of 8kPa for the first layer (using Eq. 10) and about 32-

356 120kPa for the second layer (using Eq. 9). These values compare well with the calculated

357 values from FO in Figure 7, which suggest around 20kPa for the first layer and about 10-

358 120kPa for the second layer. If one was to back calculate the values of α and β, then, the

359 first layer would yield a value of β=0.5 (whereas Eq. 10 yields β=0.2) and layers 2-4 would

360 yield values of α=0.9, 0.89, 0.1 respectively (whereas the common assumption is 0.5

361 (Tomlinson 1997)).

362 Similarly, when calculating the ultimate base capacity, one would obtain about 2MPa when

363 using Eq. 11 (i.e. based on S_u) and about 25MPa when using Eq. 12 (i.e. based on c and

364 φ). These values are different and below and well above the (linear) 6MPa that was

365 observed from the FOs during this test respectively. This is unexpected and it could be due

366 to a number of possible reasons, e.g. it may suggest that the relation usually used for the

367 pile base bearing capacity (Eq. 11) might be significantly unconservative or it may suggest

368   that the material parameter values used to calculate σ'_{v0} were too small. Nevertheless, it is

369   observed here that Eq. 11 (i.e. S_u) provides a better estimate.

370   The ability to fit a numerical model to the monitoring data (in particular, the continuous

371   vertical displacement profile) to further understand the behaviour of piles is a great

372   advantage. More confidence in the results of the back-analysed model is built when a

373   continuous strain profile is available which can show the full picture of the strains over the

374   whole length of the pile and by direct integration it may give reliable estimates of pile

375   displacements. Finally, the benefits of obtaining such a relevant numerical model can include

376   the development of load transfer curves derived from the calculated shaft friction with

377   respect to the vertical displacement.

378   **4. Case study 2: Pile load test at East Village, London.**

379   **4.1. Description of pile test**

380   The second case study considers a pile test at East Village (former Athletes Village) in

381   Stratford, London. The examined pile is 32m long with 900mm diameter (930mm at the top

382   14m). The local soil stratigraphy consists of Made Ground, Alluvium and River Terrace

383   Deposit finishing at around 14m depth and along which the pile is covered by a 15mm-thick

384   steel casing. These layers are followed by two thick layers of Lambeth Group and Thanet

385   Sand that interface at a depth of 23m. Information about pile geometry, soil stratigraphy and

386   some basic soil properties are given in Figure 8(a). The pile test consists of a static

387   maintained load applied at the top of the pile following two cycles of loading-unloading until

388   the pile fails. Details about the pile test sequence are shown in Figure 8(b). Similar to the

389   previous case, the pile was instrumented with distributed FO cables and discrete VWSGs;

390   the latter were installed at various locations along the pile depth.

391   **4.2. Data Interpretation**

392   Figure 9 (a)(b) show the monitored axial strains and the calculated axial force in the pile for

393   three selected load stages from both the FOs and the VWSGs. Similar to the previous case,

394   although the FOs show some scatter in the data, a good agreement is obtained between the

395   two sensors for both strains and forces. Observed strains and forces are roughly constant for

396   the first 14m which suggests that minor shaft friction is developed over that depth. This was

397   expected as the pile is surrounded by a steel casing at the top 14m. Moreover, at depths

398   below 14m, the axial strains and forces drop, which is due to the interaction with the

399   surrounding soil and the developed soil-pile interface friction. Additionally, on the same

400   graphs, the results of a simple FE analysis (similar to the one used in the first case, see

401   Appendix A for more details and model parameters) are included (the strain step in the first

402   figure is due to the change of pile diameter and hence the axial stiffness EA). This analysis

403   was conducted to match the observed axial strains and vertical displacements in Figure 9 (a)

404   and (c). The latter figure shows that the vertical displacements obtained by the direct

405   integration of the observed axial strains match the displacements resulting from the FE

406   model that reproduces the axial strains.

407   Figure 10 (a) shows the calculated shaft friction, SF, profiles for the three selected load

408   cases as these were determined from the FE analysis. Again, these were obtained from the

409   FE model that was calibrated to reproduce accurately the monitored axial strain and vertical

410   displacements from FOs (see Figure 9). Furthermore, Figure 10(b)(c) show the evolution of

411   SF with the applied load, P, and the 'local' vertical displacement, u, at three selected depths

412   along the pile, according to the local soil stratigraphy, i.e. in the shallow layers (covered with

413   pile casing), Lambeth Group and Thanet Sand. It is firstly observed that the first layer, which

414   is covered by the pile casing does not show significant development of strains and

415   approximately reaches an ultimate value of SF of about 40kPa. In contrast, Lambeth Group

416   and Thanet Sand do exhibit a larger development of SF that reaches around 200kPa and

417   110kPa respectively. This difference was expected as the pile in the latter two layers was not

418   covered with a steel casing and therefore pile-soil interaction friction develops resisting the

419   pile movement. In general, as expected, the SF development curves show an initial stiffness

420   that drops with the displacement, due to the plastic deformation of the soil close to the pile

421 shaft. Finally, it is again shown that SF is mobilised early in the test, whereas the pile base

422 pressure in mobilised at later stages for higher loads.

423 Finally, Figure 10 (d) shows the relevant design t-z and q-z curves following the API (2002)

424 methodology. Although there are some differences between the observed (Figure 10 (c))

425 and design (Figure 10 (d)) curves, in general they seem to agree quite well yielding

426 comparable values of ultimate pile shaft resistance.

427

428 ### 4.3. Remarks

429 Using Eq. 9 – Eq. 12 and the geotechnical data in Figure 8 one would obtain an ultimate

430 value of shaft capacity of 29kPa for the first layer (using Eq. 10), 32-219kPa for the second

431 layer (using Eq. 9) and about 116kPa for the third layer (using Eq. 10). These values

432 compare very well with the observed values from FO in Figure 10, which suggest around

433 30kPa, 200kPa and 110kPa for the three layers.

434 If one was to back calculate the values of α and β, then, the first layer would yield a value of

435 $\beta=0.21$ (whereas Eq. 10 yields around $\beta=0.2$), layer 2 would yield a values of $\alpha=0.8$

436 (whereas the common assumption is 0.5 (Tomlinson 1997)) and the third layer a value of

437 $\beta=0.2$ (in agreement to Eq. 10 that yields around $\beta=0.2$ too). So, in the case, the β-method

438 seems to work well, whereas the appropriate value for α is slightly larger than the commonly

439 used (0.5).

440 Similarly, when calculating the ultimate base capacity, one would obtain about 27MPa using

441 Eq. 12 (i.e. based on c and φ) which is well above the (roughly linear) 12MPa that was

442 observed from the FOs during this test. Again, the relation for the base capacity seems to

443 overestimate significantly the observed pile base capacity.

5. Case study 3: Osterberg-cell pile test at Francis Crick Institute, London.

444

5.1. Description of pile test

445

446 This particular case study focuses on the behaviour of a 31.5m-long, 1500mm diameter

447 bored pile during a preliminary load test at the Francis Crick Institute. This is a biomedical

448 research centre situated next to St. Pancras International train station in the London

449 Borough of Camden. One of the key differences from the previous case studies is the

450 loading mechanism. Bi-directional Osterberg Cells (O-Cell) (Osterberg 1984) were used to

451 apply load from the bottom of the pile. Figure 11(a) shows the geometry of the pile and the

452 local stratigraphy; the ground consists of two thick layers of London Clay and Lambeth

453 Group, with varying undrained strength, overlying Thanet Sand.

454 Similar to the previous case study, Fujikura reinforced ribbon cable (JBT-03813) and 8 core

455 single mode fibre (205-301 Excel OS1 8C 9/125 Loose Tube LSOH Black) were used for

456 measuring strain and temperature respectively. The installation process was identical to

457 case study 1 where both fibre optic cables were routed along opposite sides of the

458 reinforcement cage from the pile head to the top of O-Cell where a 10m long reference loop

459 was located. A pre-strain of 2000$\mu\varepsilon$ was induced in the strain cable during installation.

460 Anchorage was provided by IC-ROC clamps manufactured by Fujikura. To serve as a

461 comparison, 5 levels of VWSG were installed at 5 levels along the pile depth. The pile test

462 consisted of a single load cycle reaching a maximum of 8.33MN after 7 loading steps and

463 then unloading to zero after 3 steps, as shown in Figure 11 (b).

5.2. Data Interpretation

464

465 Figure 12(a) shows the measured axial strain profiles of the pile for three selected load

466 stages from FO and VWSGs. Considering firstly the VWSGs only, it is shown that, as

467 expected, large values of strain occur at the bottom of the pile (close to the O-cell) and

468 smaller values occur at the top. Interestingly, at a depth of about 19m, there is a significantly

469 higher value of VWSG strain which, in practice, could be considered as not representative of

470 the actual strains in the pile and therefore ignored and discarded by the design engineers.

18

471 Eliminating outliers that do not conform to the expected ranges is common in data

472 interpretation as instrument malfunctions do occur occasionally. Signs of VWSG malfunction

473 may not always be clear and these anomalies can be caused by a number of scenarios such

474 as cable damage. In some cases the recorded data is in fact a true representation which can

475 be attributed to changes in ground conditions and construction quality.

476 However, it is observed that the fibre optic cable picks some unexpectedly high values of

477 strain at a depth of about 18-23m. This is unexpected when the pile diameter is uniform at

478 that depth and therefore no step is expected in the axial strains. The data indicates that the

479 pile sustained high localised strains in that region. Similarities in trend for both systems

480 triggered a further investigation into the soil strata where the nearest borehole log (BH04)

481 (distance ~10m) recorded a change in soil layers from lignite beds and lower mottled beds in

482 the Lambeth group at around 18-19m depth. Although such a scenario was not reported in

483 the construction records, the presence of sandy glauconitic clay may have caused a

484 localised collapse during the construction of the pile which may have caused necking of the

485 pile (smaller cross-section). Subsequently, the cross sectional area, A, as well as the

486 integrity of the concrete (e.g. Young's modulus, E) at this location would have been

487 compromised. Therefore, a much higher strain reading would be very likely ($\varepsilon_a = F_a/EA$).

488 Computing the axial force by multiplying the axial strains with a constant axial stiffness, EA,

489 would therefore be unrealistic. Here, a FE model was employed again in which the axial

490 rigidity, EA, of the pile was kept constant along the pile depth, except at depth of 18-23m at

491 which it was reduced. After a parametric study, it was found that, when EA at that location

492 was reduced down to 35% of the initial EA (using again E=30000MPa and $A=0.25\pi d^2$,

493 where d is the design diameter shown in Figure 11), a good match was obtained between

494 the axial strains (Figure 12 (a)) and the vertical displacements (Figure 12 (c)). This apparent

495 reduction in EA could be due to some pile necking (smaller A) or some mixing of the pile

496 concrete with adjacent ground materials (smaller E). Then, using the results of the FE

497 model, the axial force profiles in the pile were calculated by multiplying the axial strains by

498   EA everywhere except at depth 18-23m where 0.35EA was used. The latter profiles are

499   shown in Figure 11 (b) along with the axial force from the FE model. It is shown that a good

500   comparison was obtained between the two monitoring instruments and the relevant

501   numerical analysis. As it may be observed the axial force profiles with the non-uniform EA

502   vary smoothly with the depth (in contrast to the axial strain profiles) and this is expected

503   because of force equilibrium (since the soil spring stiffness values have not been changed).

504   It is appreciated here that the use of 0.35EA for the pile analysis is not ideal and it was

505   literally obtained from a back-analysis matching the observed strain profiles. Perhaps

506   another option would be to conduct a series of solid FE analyses (e.g. 2D axisymmetric)

507   which consider different values of reduced E (of blended concrete and soil) and reduced A

508   (i.e. reduced d^2).

509   Figure 13 (a) shows the calculated shaft friction, SF, profiles for the three chosen values of

510   applied load, from the FE analysis. Again, these were obtained from the FE model that

511   reproduced accurately the monitored axial strain and vertical displacements from FOs (see

512   Figure 12). Furthermore, Figure 13(b)(c) show the evolution of SF with the applied load, P,

513   and the 'local' vertical displacement, u, at two selected depths along the pile, according to

514   the local soil stratigraphy, i.e. in the London Clay and the Lambeth Group. It is shown that

515   Lambeth Group which is deeper and closer to the O-cell exhibits early development of shaft

516   friction with the applied load, P, and that it has a stiffer response than the upper London

517   Clay, which seems to reach a SF plateau of about 35kPa at about 0.01m displacement. In

518   contrast, Lambeth Group shows an increasing development of SF which has not reached an

519   ultimate value in this test.

520   Finally, Figure 13 (d) shows the relevant design t-z curves following the API (2002)

521   methodology. Once again, although there are some differences between the observed

522   (Figure 13 (c)) and design (Figure 13 (d)) curves, in general they seem to agree quite well

523   providing similar values of ultimate pile shaft resistance.

5.3. Remarks

The monitoring data from the FO cables agree very well with the monitoring data from the VWSG. Moreover, the continuity of the FO data is able to highlight a region of localised high strain development which spreads over 6-8m in the pile shaft. A high value of strain was also captured by the VWSG sensors at the same depth, but as this was only a single value it could easily have been ignored and its significant difference from the other data points be erroneously attributed to instrument malfunction. However, the presence of continuous FO data here was able to support the localised high values of strain which might be due to some low quality concrete material of the pile or some mixing of ground material with pile concrete.

Moreover, the availability of these monitoring data allows the derivation of shaft friction development curves with the applied load or vertical displacement. These curves show that the developed shaft friction in the deeper soil layers (e.g. Lambeth Group), i.e. closer to the O-cell is, as expected, higher than the corresponding friction at the top of the pile, close to the ground surface.

Using Eq. 9 (i.e. based on S_u) and the geotechnical data in Figure 11 one would obtain an ultimate value of shaft capacity of 23-98kPa for the first layer and about 100-121kPa for the second layer. These values compare well with the observed values from FO in Figure 13, which suggest average values of around 30kPa and 150kPa for the two layers. It is shown that the shaft friction values interpreted from the observed FO data are very close to the expected design based on Eq. 9. Finally, if one was to back calculate the values of α in Eq. 9, then, the two layers would yield values of α=0.25 and α=0.68 respectively (whereas the common assumption is 0.5 (Tomlinson 1997)).

6. Conclusions

This paper presents the application of distributed fibre optic strain measurement technology for monitoring the actual field behaviour of axially loaded piles. The fibre optic data from three representative case studies of pile load tests conducted recently in London are

21

550　analysed and compared to spatially-discrete point VWSGs and relevant simple finite-element

551　analyses. The main findings of this study are the following:

552　　• The BOTDR distributed monitoring system is able to provide a continuous profile of

553　　　the induced strain within piles and this offers more confidence in determining the

554　　　developed shaft friction profiles along the pile. It is also shown that the availability of

555　　　continuous strain measurements offers a clear view of the condition of the entire pile

556　　　and hence provides an indication of any localised regions of weakness, shaft area

557　　　inhomogeneity or strain concentration. This is clearly a limitation of discrete

558　　　monitoring systems such as VWSG, which do not provide adequate information for

559　　　the whole length of the pile.

560

561　　• The distributed FO data can provide reliable information about vertical pile

562　　　displacements by direct integration of the spatially-continuous strain data. The

563　　　calculated displacements from the FO strains were verified against the

564　　　displacements obtained from a relevant FE model. It was found that such vertical

565　　　displacement profiles are very useful in calibrating the model parameters of a FE

566　　　model.

567

568　　• An available and reliable set of monitoring data over the whole length of the pile

569　　　allows an estimation of the shaft friction development curves with the applied load or

570　　　vertical displacement (load-transfer) which may be used in future design of piles in a

571　　　similar geographical region and soil stratigraphy.

572

573　　• The obtained values of shaft friction and base resistance were compared with

574　　　expected values from existing methods of geotechnical design (e.g. α and β-

575　　　methods) and were generally found to be in good agreement. The "observed" values

576　　　　of α and β were back-analysed and were also found to be, in general, in good

577　　　　agreement with the suggested values from the literature.

578

579　　• The obtained load-transfer (t-z and q-z) curves were compared with design curves

580　　　　from the literature (API). Although notable differences were observed regarding the

581　　　　pile base curves, the pile shaft curves were generally in good agreement.

591　**Nomenclature**

592　A – pile cross-sectional area

593　C_E – optical fibre parameter

594　C_T – optical fibre parameter

595　C_{TT} – optical fibre parameter

596　d – nonlinear model degradation parameter

597　D – pile diameter

598　E – pile Young's modulus

599   F_a – axial pile force

600   h – nonlinear model hardening parameter

601   k_m – nonlinear model maximum subgrade modulus parameter

602   L – total length of pile

603   M – optical fibre strain coefficient

604   N – optical fibre temperature coefficient

605   N_c – pile end bearing capacity factor

606   n_f – fibre core refractive index

607   P – top load value

608   q_b – pile base pressure

609   r – pile radius

610   SF – shaft friction

611   S_u – undrained soil shear strength

612   t – nonlinear model shear stress parameter

613   t_m – nonlinear model maximum shear stress parameter

614   u – vertical displacement

615   v_α – acoustic velocity in the optical fibre

616   v_b – central Brillouin frequency

617   v_{b0} – central Brillouin frequency at zero strain and temperature difference

618   y – depth

619   z – local vertical displacement

620   α – adhesion factor

621   ΔT – temperature change

622   Δv_{bS} – Brillouin frequency change reading from "strain cable"

623   Δv_{bT} – Brillouin frequency change reading from "temperature cable"

624   γ – soil unit weight

625   ε_a – axial pile strain

626   ε_{mech} – mechanical strain

627   ε_{real} – real (observed) strain

628   ε_{temp} – thermal expansion strain

629   λ_l – wavelength of the input light

630   v – Poisson's ratio

631   **References**

632   Abchir, Z, Burlon, S, Frank, R, Habert, J & Legrand, S 2015, 't–z curves for piles from

633   pressuremeter test results', *Géotechnique*, vol 66, no. 2, pp. 137-148.

634   Acikgoz, MS, Pelecanos, L, Giardina, G, Aitken, J & Soga, K 2017, 'Distributed sensing of a

635   masonry vault during nearby piling', *Structural Control and Health Monitoring*, vol 24, no. 3,

636   p. e1872.

637   Acikgoz, MS, Pelecanos, L, Giardina, G & Soga, K 2016, 'Field monitoring of piling effects

638   on a nearby masonry vault using distributed sensing.', *International Conference of Smart*

639   *Infrastructure and Construction*, ICE Publishing, Cambridge.

API 2002, 'API Recommended Practice. Planning, Designing and Constructng Fixed Offshore Platforms - Working Stress Design', American Petroleum Institute, 2A-WSD, American Petroleum Institute.

Bathe, KJ 1996, *Finite Element Procedures*, 1st edn, Prentice Hall, New Jersey.

Berezantzev, VG, Khristoforov, VS & Golubkov, VN 1961, 'Load bearing capacity and deformation of piled foundations', *Proc. 5th Int. Conf. on Soil Mechanics and Foundation Engineering*, Paris.

Bustamante, M & Gianeselli, L 1982, 'Pile bearing capacity predictions by means of static', *Proc., 2nd European Symp. on Penetration Testing*, Amsterdam.

Butterfield, R & Banergee, PK 1971, 'The elastic analysis of compressible piles and pile groups', *Geotechnque*, vol 21, no. 1, pp. 43-60.

Cheung, L, Soga, K, Bennett, PJ, Kobayashi, Y, Amatya, B & Wright, P 2010, 'Optical fibre strain measurement for tunnel lining monitoring', *Proceedings of the ICE - Geotechnical Engineering*, vol 163, no. 3, pp. 119-130.

Comodromos, EM & Bareka, SV 2009, 'Response evaluation of axially loaded fixed-head pile groups in clayey soils', *International Journal for Numerical and Analytical Methods in Geomechanics*, vol 33, no. 17, pp. 1839-1865.

de Battista, N, Elshafie, MZEB, Soga, K, Williamson, M, Hazelden, G & Hsu, YS 2015, 'Strain monitoring using embedded distributed fibre optic sensors in a sprayed concrete tunnel lining during the excavation of cross-passages', 7th International Conference on Structural Health Monitoring and Intelligent Infrastructure (SHMII7), Torino, Italy.

de Battista, N, Kechavarzi, C, Seo, H, Soga, K & Pennington, S 2016, 'Distributed fibre optic sensors for measuring strain and temperature of cast-in-situ concrete test piles',

663 *Proceedings of the International Conference on Smart Infrastructure and Construction*

664 *(ICSIC)*, Thomas Telford, Cambridge, UK.

665 Di Murro, V, Pelecanos, L, Soga, K, Kechavarzi, C, Morton, RF & Scibile, L 2016,

666 'Distributed fibre optic long-term monitoring of concrete-lined tunnel section TT10 at CERN.',

667 *International Conference of Smart Infrastructure and Construction*, ICE Publishing,

668 Cambridge.

669 Doherty, P, Igoe, D, Murphy, G, Gavin, K, Preston, J, McAvoy, C, Byrne, BW, McAdam, R,

670 Burd, HJ, Houlsby, GT, Martin, CM, Zdravkovic, LT, Taborda, DMG, Potts, DM, Jardine, RJ,

671 Sideri, M, Schroeder, FC, Muir Wood, A, Kallehave, D & Skov Gretlund, J 2015, 'Field

672 validation of fibre Bragg grating sensors for measuring strain on driven steel piles',

673 *Géotechnique Letters*, vol 5, no. 2, pp. 74-79.

674 Eslami, A & Fellenius, BH 1997, 'Pile capacity by direct CPT and CPTU methods applied to

675 102 case histories', *Can. Geotech. J*, vol 34, pp. 886-904.

676 Fellenius, BH 1989, 'Prediction of pile capacity', *ASCE Symposium on Predicted and*

677 *Observed Behavior of Piles*.

678 Frank, R & Zhao, SR 1982, 'Estimating the Settlement of Axially Loaded Bored Piles in Fine

679 Sand by PMT Data', *Bull. Liaison LPC*, vol 119.

680 Goldfeld, Y & Klar, A 2013, 'Damage Identification in Reinforced Concrete Beams Using

681 Spatially Distributed Strain Measurements', *Journal of Structural Engineering*, vol 139, no.

682 12, pp. 1-11.

683 Hauswirth, D, Puzrin, AM, Carrera, A, Standing, JR & Wan, MSP 2014, 'Use of fibre-optic

684 sensors for simple assessment of ground surface displacements during tunnelling',

685 *Geotechnique*, vol 64, no. 10, pp. 837-842.

27

686 Horiguchi, T, Shimizu, K, Kurashima, T, Tateda, M & Koyamada, Y 1995, 'Development of a

687 distributed sensing technique using Brillouin scattering', *Journal of Light-wave Technology*,

688 vol 13, no. 7, pp. 1296-1302.

689 Iten, M 2011, 'Novel applications of distributed fiber-optic sensing in geotechnical

690 engineering', PhD Thesis, ETH, Zurich.

691 Jardine, RJ & Chow, FC 1996, 'New design methods for offshore piles', MTD, Centre for

692 Petroleum and Marine Technology (CPMT), 96/103, London.

693 Kechavarzi, C, Soga, K, de Battista, N, Pelecanos, L, Elshafie, MZEB & Mair, RJ 2016,

694 *Distributed Fibre Optic Strain Sensing for Monitoring Civil Infrastructure*, Thomas Telford,

695 London.

696 Kersey, AD & Morey, WW 1993, 'Multiplexed Bragg grating fibre-laser strain-sensor system

697 with mode-locked interrogation', *Electron. Lett*, vol 29, no. 1, pp. 112-114.

698 Kitiyodom, P & Matsumoto, T 2003, 'A simplified analysis method for piled raft foundations in

699 non-homogeneous soils.', *International Journal for Numerical and Analytical Methods in*

700 *Geomechanics*, vol 27, pp. 85-109.

701 Klar, A, Bennett, PJ, Soga, K, Mair, RJ, Tester, P, Fernie, R, St John, HD & Thorp-Peterson,

702 G 2006, 'Distributed strain measurement for pile foundations', *Proceedings of the ICE -*

703 *Geotechnical Engineering*, vol 159, no. 3, pp. 135-144.

704 Klar, A, Dromy, I & Linker, R 2014, 'Monitoring tunneling induced ground displacements

705 using distributed fiber-optic sensing', *Tunnelling and Underground Space Technology*, vol

706 40, pp. 141-150.

707 Knappett, JA & Craig, RF 2012, *Craig's Soil Mechanics*, 8th edn, CRC Press, London.

708 Kraft, ML, Ray, RP & Kakaaki, T 1981, 'Theoretical t-z curves', *J. Geotech. Engrg. Div.*

709 *ASCE*, vol 107, no. 11, pp. 1543-1561.

710 Kulhawy, FH & Prakoso, WA 1999, 'Discussion of "End Bearing Capacity of Drilled Shafts in
711 Rock', *J. Geotech Eng ASCE*, vol 125, no. 12, pp. 1106-1109.

712 Kurashima, T, Horiguchi, T, Izumita, H & Tateda, M 1993, 'Brillouin Optical-Fiber Time
713 Domain Reflectometry', *IEICE Transactions on Cummunications*, vol E76-B, no. 4, pp. 382-
714 390.

715 Lee, CY 1993, 'Pile group settlement analysis by hybrid layer approach', *Journal of the*
716 *Geotechnical Engineering Division, ASCE*, vol 119, no. 6, pp. 984-997.

717 Lee, W, Lee, W, Lee, S & Salgado, R 2004, 'Measurement of pile load transfer using the
718 Fiber Bragg Grating sensor system', *Canadian Geotechnical Journal*, vol 41, no. 6, pp. 1222-
719 1232.

720 Lehane, BM, Jardine, RJ, Bond, AJ & R., F 1993, 'Mechanisms of shaft friction in sand from
721 instrumented pile tests', *Journal of Geotechnical Engineering*, vol 119, no. 1, pp. 19-35.

722 Levenberg, K 1944, 'A Method for the Solution of Certain Non-Linear Problems in Least
723 Squares', *Quarterly of Applied Mathematics*, vol 2, pp. 164-168.

724 Linker, R & Klar, A 2015, 'Detection of Sinkhole Formation by Strain Profile Measurements
725 Using BOTDR: Simulation Study', *Journal of Engineering Mechanics*, pp. 1-10.

726 Liu, J & Zhang, M 2012, 'Measurement of residual force locked in open-ended pipe pile
727 using FBG-based sensors', *Electron. J. Geotech. Eng*, vol 17, pp. 2145-2154.

728 Marduardt, D 1963, 'An Algorithm for Least-Squares Estimation of Nonlinear Parameters',
729 *SIAM Journal on Applied Mathematics*, vol 11, no. 2, pp. 431-441.

730 McCabe, BA & Lehane, BM 2006, 'Behavior of Axially Loaded Pile Groups Driven in Clayey
731 Silt', *Journal of Geotechnical and Geoenvironmental Engineering*, vol 132, no. 3, pp. 401-
732 410.

733   Ménard, L 1963, 'Calcul de la force portante des fondations à partir des essais

734   pressiométriques', *Sols-Soils*, vol 6, pp. 9–27.

735   Meyerhof, GG 1965, 'Shallow foundations', *Journal of Soil Mechanics and Foundations*

736   *Division, ASCE*, vol 91, no. 2, pp. 21-31.

737   Mohamad, H 2007, 'Distributed optical fibre strain sensing of geotechnical structures. PhD

738   Thesis', University of Cambridge, Cambridge, UK.

739   Mohamad, H, Bennett, PJ, Soga, K, Mair, RJ & Bowers, K 2010, 'Behaviour of an old

740   masonry tunnel due to tunnelling-induced ground settlement', *Geotechnique*, vol 60, no. 12,

741   pp. 927-938.

742   Mohamad, H, Soga, K, Bennett, PJ, Mair, RJ & Lim, CS 2012, 'Monitoring Twin Tunnel

743   Interaction Using Distributed Optical Fiber Strain Measurements', *Journal of Geotechnical*

744   *and Geoenvironmental Engineering*, vol 138, no. 8, pp. 957-967.

745   Mohamad, H, Soga, K, Pellew, A & Bennett, PJ 2011, 'Performance Monitoring of a Secant-

746   Piled Wall Using Distributed Fiber Optic Strain Sensing', *Journal of Geotechnical and*

747   *Geoenvironmental Engineering, ASCE*, vol 137, no. 12, pp. 1236-1243.

748   Osterberg, JO 1984, 'A new simplified method for load testing drilled shafts', *Foundation*

749   *Drilling*, ADSC.

750   Ouyang, Y, Broadbent, K, Bell, A, Pelecanos, L & Soga, K 2015, 'The use of fibre optic

751   instrumentation to monitor the O-Cell load test on a single working pile in London',

752   *Proceedings of the XVI European Conference on Soil Mechanics and Geotechnical*

753   *Engineering*, Edinburgh.

754   Pelecanos, L & Soga, K 2017, 'Using distributed strain data to evaluate load-transfer curves

755   for axially loaded piles', *Journal of Geotechnical & Geoenvironmental Engineering, ASCE*

756   *(Submitted).*

757 Pelecanos, L, Soga, K, Chunge, MPM, Ouyang, Y, Kwan, V, Kechavarzi, C & Nicholson, D

758 2017, 'Distributed fibre-optic monitoring of an Osterberg-cell pile test in London.',

759 *Geotechnique Letters*, vol 7, no. 2, pp. 1-9.

760 Pelecanos, L, Soga, K, Hardy, S, Blair, A & Carter, K 2016, 'Distributed fibre optic monitoring

761 of tension piles under a basement excavation at the V&A museum in London.', *International*

762 *Conference of Smart Infrastructure and Construction*, ICE Publishing, Cambridge.

763 Poulos, HG 1989, 'Pile behaviour - theory and application', *Geotechnique*, vol 39, no. 3, pp.

764 365-415.

765 Poulos, HG & Davis, EH 1974, *Elastic solutions for soil and rock mechanics*, Wiley, New

766 York.

767 Randolph, MF 2003, 'Science and empiricism in pile foundation design', *Geotechnique*, vol

768 53, no. 10, pp. 847-875.

769 Salgado, R 2008, *The engineering of foundations*, McGraw Hill, New York.

770 Savitzky, A & Golay, MJE 1964, 'Smoothing and Differentiation of Data by Simplified Least

771 Squares Procedures', *Analytical Chemistry*, vol 36, no. 8, pp. 1627-1639.

772 Schwamb, T & Soga, K 2015, 'Numerical modelling of a deep circular excavation at Abbey

773 Mills in London', *Geotechnique*, vol 65, no. 7, pp. 604-619.

774 Schwamb, T, Soga, K, Mair, RJ, Elshafie, MZEB, R., S, Boquet, C & Greenwood, J 2014,

775 'Fibre optic monitoring of a deep circular excavation', *Proceedings of the ICE - Geotechnical*

776 *Engineering*, vol 167, no. 2, pp. 144-154.

777 Seo, H-J, Pelecanos, L, Kwon, Y-S & Lee, IM 2017, 'Net load–displacement estimation in

778 soil-nail pullout tests', *Proceedings of the Institution of Civil Engineers - Geotechnical*

779 *Engineering*, pp. 1-14.

780   Soga, K 2014, 'XII Croce Lecture: Understanding the real performance of geotechnical

781   structures using an innovative fibre optic distributed strain measurement technology', *Rivista*

782   *Italiana di Geotechnica*, vol 4, pp. 7-48.

783   Soga, K, Kechavarzi, C, Pelecanos, L, de Battista, N, Williamson, M, Gue, CY, Di Murro, V &

784   Elshafie, M 2017, 'Distributed fibre optic strain sensing for monitoring underground

785   structures - Tunnels Case Studies ', in S Pamukcu, L Cheng (eds.), *Underground Sensing*,

786   1st edn, Elsevier.

787   Soga, K, Kwan, V, Pelecanos, L, Rui, Y, Schwamb, T, Seo, H & Wilcock, M 2015, 'The role

788   of distributed sensing in understanding the engineering performance of geotechnical

789   structures', *Proceedings of the XVI European Conference on Soil Mechanics and*

790   *Geotechnical Engineering,* Edinburgh.

791   Stas, CV & Kulhawy, FH 1984, 'Critical evaluation of design methods for foundation under

792   axial uplift & compression loading', Electric Power Research Institute, EL-3771, Palo Alto.

793   Tomlinson, MJ 1997, 'The adhesion of piles driven in clay', *Proc. 4th Intern. Conf. Soil.*

794   *Mech.*, London.

795   Tomlinson, M & Woodward, J 2014, *Pile design and construction practice,* CRC Press.

796

797   **Appendix A**

798   The numerical finite element analysis used in this paper is described in Figure 14. A vertical

799   axially-loaded pile is modelled with a series of linear-elastic two-noded beam elements with

800   vertical displacement degrees-of-freedom only and a series of nonlinear springs,

801   representing the surrounding soil, attached to each node.

802 The behaviour of the soil spring is governed by a nonlinear load-transfer curve that follows

803 the Degradation and Hardening Hyperbolic Model (DHHM) model of (Pelecanos & Soga

804 2017) described by Eq. 13.

805
$$t = \frac{k_m z}{\sqrt[d]{\left(1 + \left(\frac{k_m}{t_m} z\right)^{hd}\right)}}$$

806 **Eq. 13**

807 Where k_m is the maximum stiffness for displacement, z=0 (units: [force/length^3]), t_m is the

808 "maximum" value of shear stress, t (maximum only in the case of no hardening/softening, i.e.

809 h=0) (units: [force/length^2]), d is the degradation parameter (units: [-]), that governs the

810 degradation of subgrade modulus, k, with displacement, z, and h is the hardening parameter

811 (units: [-]), that mostly governs the model behaviour at large displacements, z. It should be

812 noted here that some t-z curves (see Section 1) include the effect of the pile diameter too,

813 but in the considered cases that mostly involved London Clay and large pile diameters (i.e.

814 no significant arching) it is expected that the diameter doesn't affect the obtained t-z curves.

815 The values of the 4 parameters of the model (k_m, t_m, d, h) are obtained by matching the axial

816 strain, $\varepsilon_a(z)$, and vertical displacement, u(z), profiles resulting from the numerical model and

817 those observed in the field as shown in Figure 6 (a) (c), Figure 9 (a) (c) and Figure 12 (a) (c).

818 The equations satisfying global equilibrium of the pile-soil problem follow a standard static

819 finite element formulation (Bathe 1996) and are described by Eq. 14.

820
$$\left[K_p + K_s\right] \cdot \{u\} = \{F\}$$

821 **Eq. 14**

822 Where, [K_p] and [K_s] are the global pile and soil stiffness matrices respectively, which contain

823 information about the geometry and the material properties of the pile and soil respectively,

824 {u} is the vector of the displacement degrees-of-freedom and {F} is the vector of the

825 externally applied forces.

826   Boundary conditions applied consist only of the applied load which is specified as a known

827   value in the {F} vector; at the first node for a top-loaded pile or at the last node for a bottom-

828   loaded O-cell test. Finally, the numerical model parameters adopted for the analyses of the

829   case studies presented in this paper (which, as explained before, were obtained by matching

830   the observed pile response) are listed in Table 1.

831   **Table 1. Parameters of the numerical FE beam-spring model for all cases considered**

Case 1 – Broadgate Pile					
Layer	**Depth [m]**	**k_m [MN/m^3]**	**t_m [MN/m^2]**	**d []**	**h []**
1	0 – 6	8	0.011	2	0.8
2	6 – 12	14	0.157	0.9	1.5
3	12 – 19	16	0.136	2.5	1
4	19 – 25	2	0.008	1.2	1
Base	25	459	65573	1	1
Case 2 – East Village Pile					
Layer	**Depth [m]**	**k_m [MN/m^3]**	**t_m [MN/m^2]**	**d []**	**h []**
1	0 – 14	14	0.053	1	1
2	14 – 23	37	0.223	1	1
3	23 – 32	24	0.195	1.6	1
Base	32	513	17.113	1	1
Case 3 – Francis Crick Pile					
Layer	**Depth [m]**	**k_m [MN/m^3]**	**t_m [MN/m^2]**	**d []**	**h []**
1	0 – 21	21	0.036	3	1
2	1 – 25	57	0.117	3	0.7

832

833   **Appendix B**

834   The data used for the API (2002) curves shown in Figure 7, Figure 10, Figure 13 are listed in

835   Table 2. These curves depend only on the soil material properties and the geometry

836   (diameter, D) of the pile. The values for t_{ult} were obtained by using Eq. 9 and Eq. 10 for clay

837   and sand respectively, whereas those for q_{ult} were obtained by using Eq. 11 and Eq. 12 for

838   clay and sand respectively.

839   **Table 2. Data used for the API (2002) curves.**

t-z for sand							
z [in]	0	0.1	0.4				
t/t$_{ult}$ [-]	0	1	1				
t-z for clay							
z/D [-]	0	0.0016	0.0031	0.0057	0.008	0.01	0.02	0.03
t/t$_{ult}$ [-]	0	0.3	0.5	0.75	0.9	1	0.9	0.9
q-z for sand & clay							
z/D [-]	0	0.002	0.13	0.042	0.073	0.1	0.2	
q/q$_{\_ult}$	0	0.25	0.5	0.75	0.9	1	1	

840

841   **Figure Captions**

842   **Figure 1. Principle of distributed fibre optic sensing using BOTDR.**

843   **Figure 2. Fibre optic cables used at the pile cases studied: (a) Fujikura reinforced**
844   **"strain cable" and (b) Unitube "temperature cable".**

845   **Figure 3. Schematic illustration of FO installation and monitoring of piled foundations.**

846   **Figure 4. View of installed fibre optic cables and vibrating wire strain gauges on the**
847   **pile cage: (a) detailed view of clamp, (b) general view of installed sensors.**

848   **Figure 5. Description of Case 1 – Broadgate pile load test case: (a) pile geometry &**
849   **soil stratigraphy, (b) test schedule**

850   **Figure 6. Monitored data profiles for Case 1 – Broadgate: (a) axial strain, (b) axial**
851   **force and (c) vertical displacement.**

35

852　**Figure 7. Calculated pile shaft friction from FE analysis for Case 1 – Broadgate: (a)**
853　**shaft friction profiles, (b) shaft friction development with applied load, (c) shaft**
854　**friction development with vertical displacement, and (d) relevant API t-z and q-z**
855　**curves.**

856　**Figure 8. Description of Case 2 – East Village pile load test case: (a) pile geometry &**
857　**soil stratigraphy, (b) test schedule**

858　**Figure 9. Monitored data profiles for Case 2 – East Village: (a) axial strain, (b) axial**
859　**force and (c) vertical displacement.**

860　**Figure 10. Calculated pile shaft friction from FE analysis for Case 2 – East Village: (a)**
861　**shaft friction profiles, (b) shaft friction development with applied load, (c) shaft**
862　**friction development with vertical displacement, and (d) relevant API t-z and q-z**
863　**curves.**

864　**Figure 11. Description of Case 3 – Francis Crick pile load test case: (a) pile geometry**
865　**& soil stratigraphy, (b) test schedule**

866　**Figure 12. Monitored data profiles for Case 3 – Francis Crick: (a) axial strain, (b) axial**
867　**force and (c) vertical displacement.**

868　**Figure 13. Calculated pile shaft friction from FE analysis for Case 3 – Francis Crick:**
869　**(a) shaft friction profiles, (b) shaft friction development with applied load, (c) shaft**
870　**friction development with vertical displacement, and (d) relevant API t-z curves.**

871　**Figure 14. Numerical analysis model of pile-soil interaction: (a) pile, (b) axial strain**
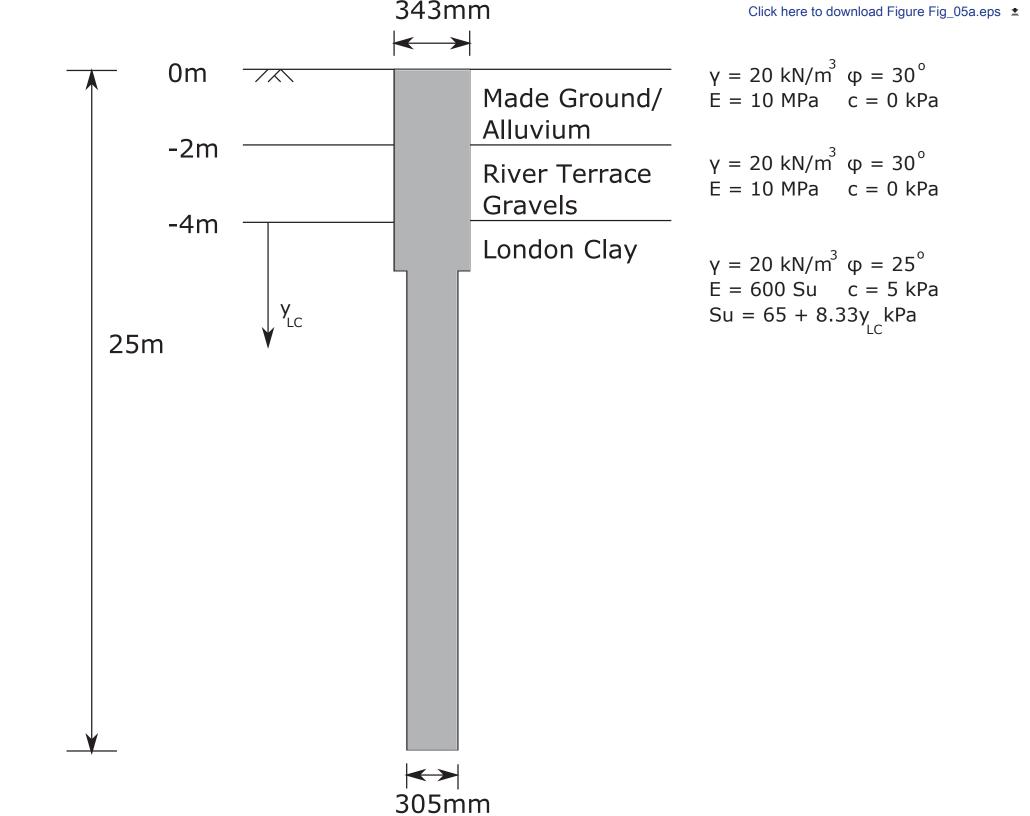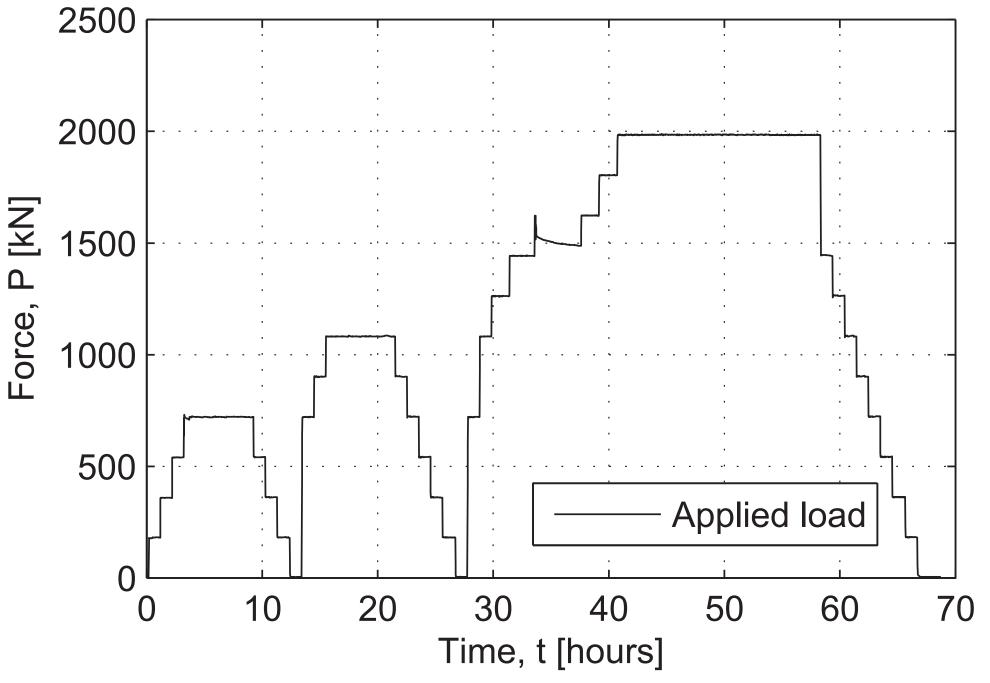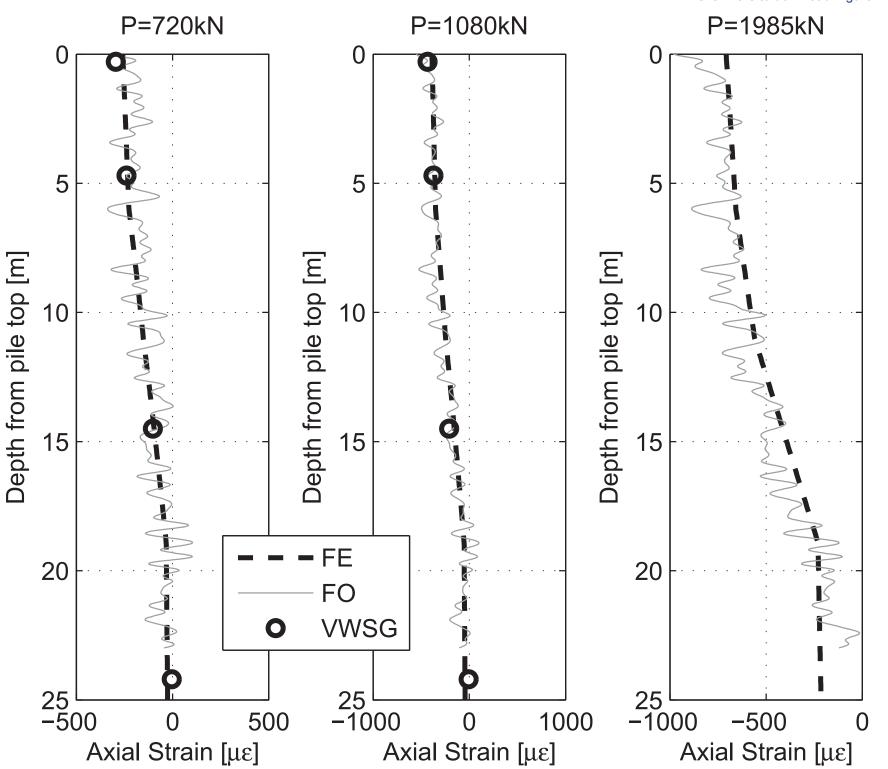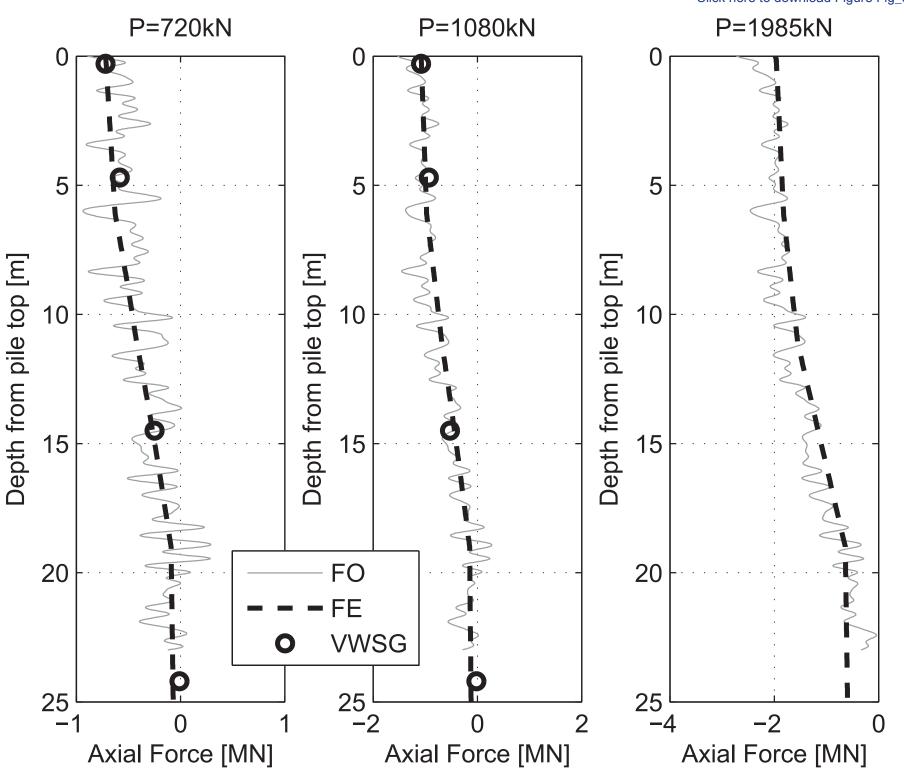872　**distribution, (c) top load-displacement, (d) numerical beam-spring model and (e) load-**
873　**transfer curve.**

874

BOTDR

Pump Laser

optical pulse input

incident light

back scattered light

strain: ε_0

applied strain: ε_1

strain: ε_0

ν_{B1}

ν_{B0}

Brillouin Frequency [GHz]

Scattered Light Power

z_1

z_2

Cable Distance [m]

Steel wire

4x125μm optical fibres
with 250μm coating

Strong nylon

1.2mm

5.2mm

Gel-filled tube

Water blocking
Glass Yarns

PE
(polyethylene)
outer Sheath

Optical fibre

6.9mm

bottom steel cage

ground

FO cables

higher
steel
cage

ground

FO cables

FO analyser
machine

FO cables

ground

343mm

0m — Made Ground/Alluvium

$\gamma = 20$ kN/m^3 $\varphi = 30^\circ$
$E = 10$ MPa $c = 0$ kPa

-2m — River Terrace Gravels

$\gamma = 20$ kN/m^3 $\varphi = 30^\circ$
$E = 10$ MPa $c = 0$ kPa

-4m — London Clay

$\gamma = 20$ kN/m^3 $\varphi = 25^\circ$
$E = 600$ Su $c = 5$ kPa
Su $= 65 + 8.33 y_{LC}$ kPa

y_{LC}

25m

305mm

Broadgate pile test

930mm

0m

Made Ground

c = 18 kPa φ = 27°

-10m

Alluvium

c = 36 kPa φ = 35°

-11m

River Terrace Gravels c = 31 kPa φ = 33°

-14m

Lambeth Group

Su = 63-438 kPa

32m

-23m

Thanet Sand

c = 29 kPa φ = 36°

900mm

East Village pile test

0m

Made Ground

-4m

y_1

Weathered
London Clay

-8m

London Clay
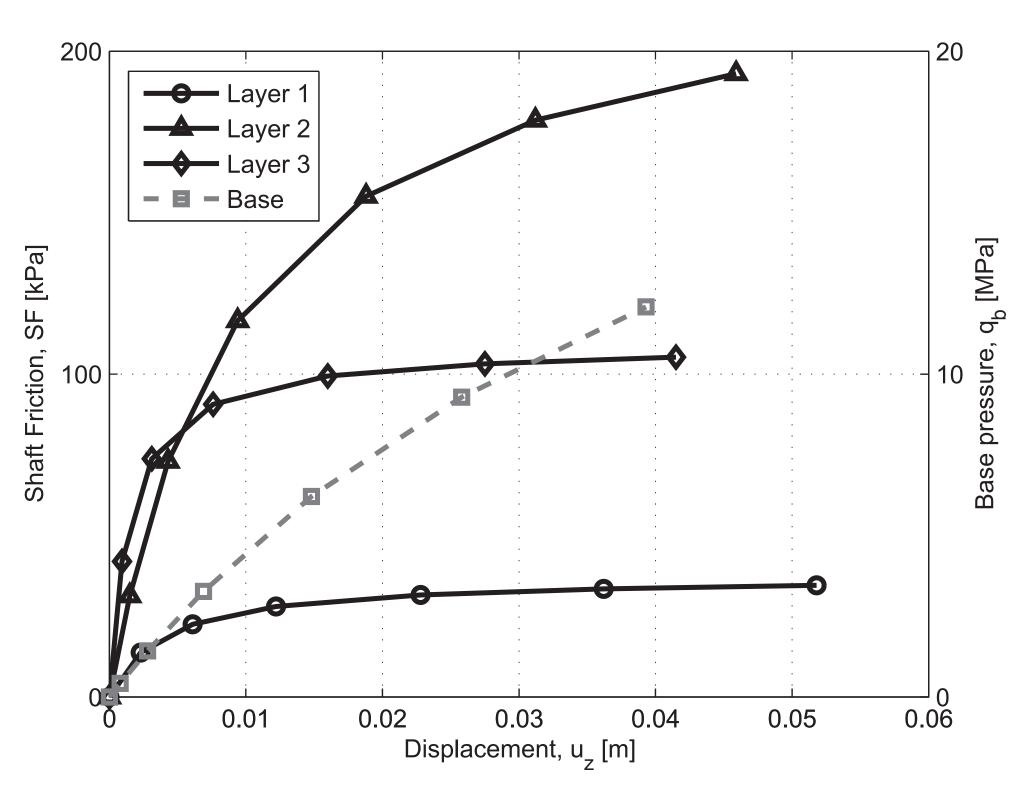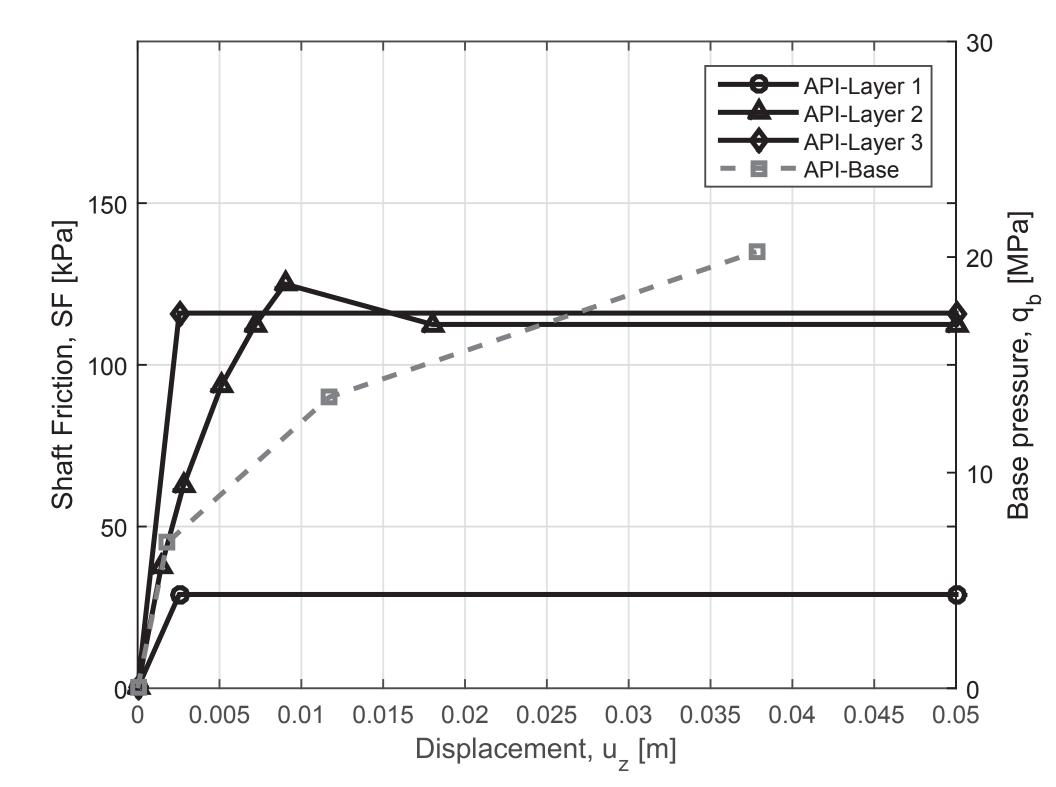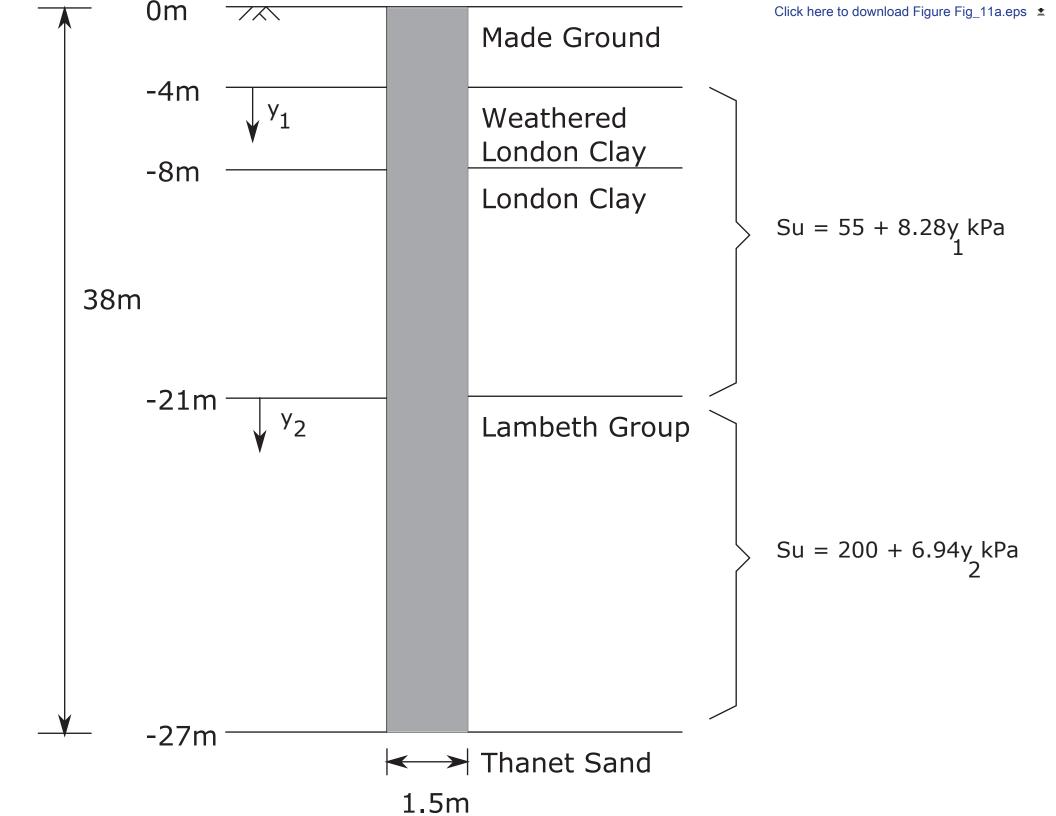
38m

$Su = 55 + 8.28y_1$ kPa

-21m

y_2

Lambeth Group

$Su = 200 + 6.94y_2$ kPa

-27m

Thanet Sand

1.5m

Francis Crick pile test

P

y

ε(y)

y

P

u

P

t

z

(a)

(b)

(c)

(d)

(e)